Journal of Materials Science & Technology 152 (2023) 190–200

Contents lists available at ScienceDirect

Journal of Materials Science & Technology

journal homepage: www.elsevier.com/locate/jmst

Research Article

A novel cobalt-free oxide dispersion strengthened medium-entropy alloy with outstanding mechanical properties and irradiation resistance

Ao Fu[a], Bin Liu[a,*], Bo Liu[b], Yuankui Cao[a], Jian Wang[a], Tao Liao[a], Jia Li[c], Qihong Fang[c], Peter K. Liaw[d], Yong Liu[a]

[a] State Key Laboratory of Powder Metallurgy, Central South University, Changsha 410083, China
[b] Key Laboratory of Radiation Physics and Technology of Ministry of Education, Institute of Nuclear Science and Technology, Sichuan University, Chengdu 610064, China
[c] State Key Lab of Advanced Design and Manufacturing for Vehicle Body, Hunan University, Changsha 410082, China
[d] Department of Materials Science and Engineering, The University of Tennessee, Knoxville, TN 37996, USA

ARTICLE INFO

Article history:
Received 14 October 2022
Revised 22 November 2022
Accepted 22 November 2022
Available online 15 February 2023

Keywords:
Medium-entropy alloys
Irradiation
Oxide nanoparticles
Strength
Deformation mechanism

ABSTRACT

A novel cobalt-free oxide dispersion strengthened (ODS) equiatomic FeCrNi medium entropy alloy (MEA) was successfully fabricated through mechanical alloying and hot extrusion (HE). The ODS FeCrNi MEA is composed of a single face-centered cubic (FCC) matrix, in which highly dispersed oxide nanoparticles, including $Y_2Ti_2O_7$, Y_2TiO_5 and Y_2O_3, are uniformly distributed. Compared with the FeCrNi MEA, the ODS FeCrNi MEA exhibits the improved yield strength (1120 MPa) and ultimate tensile strength (1274 MPa) with adequate ductility retention (12.1%). Theoretical analysis of the strengthening mechanism indicates that the high strength is mainly attributed to the grain-boundary strengthening caused by fine grains and the precipitation strengthening resulted from the oxide nanoparticles. Meanwhile, the matrix that easily activates mechanical twinning during the deformation process is the main reason to ensure moderate ductility. In addition, the introduction of high-density oxide nanoparticles can disperse the defect distribution and suppress the defect growth and irradiation-induced segregation, leading to the excellent irradiation resistance. These findings provide innovative guidance for the development of high-performance structural materials for future nuclear energy applications with balanced strength and ductility.

1. Introduction

Structural materials used in the fourth-generation fission or fusion reactors require extraordinary comprehensive properties because of the extremely harsh service environment, such as the higher operation temperature (300 - 800 °C) and greater irradiation neutron dose (100 - 200 dpa) [1–6]. Austenitic steels are widely used as structural materials in the current water-cooled nuclear fission reactors, but they do not exhibit sufficient irradiation resistance in the next-generation nuclear energy system, where a series of problems, such as void swelling and irradiation-induced segregation, can occur [3–5]. Ferritic/martensitic steels generally have higher void swelling resistance than austenitic steels, while their thermal stability and creep resistance are low at temperature above 550 °C [4,5]. Recently, medium/high entropy alloys (MEAs/HEAs) based on three or more principal elements have been proposed, which exhibit outstanding irradiation tolerance than conventional steels [5–7]. Moreover, MEAs/HEAs also display superior physical and mechanical properties, such as high thermodynamic stability, great fracture toughness, etc., [4,5], making them promising candidates for nuclear energy applications. However, the relatively low strength at elevated temperatures is one of the prominent shortages for the MEAs/HEAs. Therefore, how to further improve the strength without dramatic sacrifice in the ductility of the MEAs/HEAs become particularly important.

Introducing oxide nanoparticles, such as Al_2O_3, Y_2O_3, $Y_2Ti_2O_7$, etc., into the metallic materials has been considered as an effective approach to improve the strength by generating fine grains and restricting dislocation motion [8–12]. In comparison with the casting route, the powder metallurgy (P/M) technique is reported to be a more promising way for preparing the oxide dispersion strengthened (ODS) materials, because it can promote the in-situ formation of highly dispersed oxide nanoparticles [8,13]. The P/M technique

* Corresponding author.
E-mail address: binliu@csu.edu.cn (B. Liu).

https://doi.org/10.1016/j.jmst.2022.11.061
1005-0302/

can also help refine the grains, stabilize the phase structure, and avoid the elemental segregation, thereby obtaining more excellent mechanical properties [8–10]. For example, Guo et al. [8] prepared $Y_2Ti_2O_7$-nanoparticles-enhanced FeCoNi MEA by mechanical alloying and spark plasma sintering (SPS). Compared with the FeCoNi MEA, the grain size of the ODS FeCoNi MEA was refined from 0.735 to 0.237 μm. The compressive yield strength increases by 57% and 22% at room temperature and 700 °C, respectively. Hadraba et al. [9] fabricated the Y_2O_3-nanoparticles-enhanced CoCrFeMnNi HEA and found that the compressive yield strength reaches 1232 MPa at room temperature. Further study reported by Dobeš et al. [10] suggests that the ODS CoCrFeMnNi HEA exhibits higher creep strength than some conventional ODS alloys, such as ODS Cu and ODS Fe-Cr, at temperatures from 700 to 800 °C. These results suggest that the ODS MEAs/HEAs can overcome the strength-ductility trade-off in a wide temperature range. Despite these efforts, the studies about ODS MEAs/HEAs seem somewhat sketchy, and mainly focus on enhancing the mechanical properties or investigating the size, distribution, volume fraction, crystal structure and chemical composition of the oxide nanoparticles [8,9]. There are very few studies available regarding the possible influences of oxide nanoparticles on strengthening mechanism and deformation behavior. Besides, oxide nanoparticles also provide many additional interfaces that can act as preferential stable sinks for irradiation defects, such as dislocation loops, voids and helium bubbles, which is beneficial for improvement of irradiation-induced hardening and embrittlement [6]. However, very limited researches have been reported on the irradiation resistance of the ODS MEAs/HEAs.

Here, a novel Co-free FeCrNi MEA was selected as the base alloy because of its excellent strength-ductility combination and corrosion resistance [14,15], and the elimination of cobalt-induced high radioactivity under neutrons irradiation [5,16]. Minor Y and Ti were incorporated into the matrix to induce the in-situ formation of highly- dispersed oxide nanoparticles via mechanical alloying and hot extrusion (HE). The products prepared by HE have many advantages, such as the large product dimension, compact microstructure, and excellent mechanical properties, compared with those prepared by SPS [17,18]. The details of oxide nanoparticles were characterized, and the mechanical properties at different temperatures were tested. The effect of oxide nanoparticles on strengthening mechanism, deformation and irradiation behaviors is systematically analyzed. This work aims at obtaining a novel cobalt-free ODS MEA with a good combination of mechanical properties and irradiation resistance.

2. Experimental procedures

The equiatomic FeCrNi powders were fabricated via a gas-atomization method in high-purity argon. Then the gas-atomized powders were blended with TiH_2 and YH_3 powders in a planetary ball-miller with a nominal composition of FeCrNi-0.3TiH_2–0.3YH_3 (weight percent, wt.%), followed by mechanical milling for 12 h at 300 rpm under an argon atmosphere with a ball-to-powder mass ratio of 10:1. Subsequently, the as-milled powders were encapsulated into a stainless steel can. Finally, the encapsulated can was pre-heated at 1150 °C for 1 h, and immediately hot extruded to a bar with an extrusion ratio of 7:1. The chemical composition of the bar was detected to be $Fe_{34.01}Cr_{32.47}Ni_{32.96}Y_{0.21}Ti_{0.35}O_{0.5926}$ (wt.%). During mechanical alloying and HE processes, the hydrides can react with dissolved oxygen atoms in the raw materials to in-situ form oxides. Generally, the oxides formed by the in-situ method are smaller in size and have a cleaner phase interface with the matrix than the directly added oxides (an ex-situ method) [13].

Cylindrical dog-bone shaped tensile specimens and irradiation specimens (Φ 10 mm × 3 mm) were cut along the extrusion direction. Tensile tests were performed on an Instron 3369 testing machine at 25, 600, 700, and 800 °C, respectively, with a loading strain rate of 1×10^{-3} s^{-1}. Irradiation specimens were irradiated with 7.5 MeV Au ions to a fluence of 5×10^{16} Au ions/cm^2 at room temperature. The irradiation tests were performed on the implantation system at Southwest Institute of Physics of China. The corresponding data of damage depth, Au ions concentration and damage dose in displacements per atom (dpa) were obtained from SRIM 2008 with the full cascade TRIM simulation code. Specimens for microstructural characterization was also sectioned along the extrusion direction.

The average particle size of the powders was measured by a laser particle size distribution analyzer (LPSDA, LMS-30). Chemical composition was determined by an inductively coupled plasma mass spectrometry (ICP-MS) analysis and a Leco O/N analyzer (LecoTC463). Phase analysis was performed by an X-ray diffractometer (XRD, D/max-2550). The microstructure was observed by a double-beam scanning electron microscopy (SEM, Helios Nanolab 600i) equipped with an electron backscatter diffraction (EBSD) device. Needle-shaped specimens required for atom probe tomography (APT) characterization were fabricated by a focused ion beam (FIB) instrument. The APT observation was performed by a local electrode atom probe (CAMEACA LEAP 5000XR). Imago Visualization and Analysis Software (IVAS 3.8) were used for three-dimensional (3D) atomic reconstruction. Specimens for transmission electron microscope (TEM) observation prepared by a double-jet electrochemical polisher or a FIB instrument. The TEM observation was conducted on a FEI Tecnai G^2 F20 operated at 200 kV. Average particle size and volume fraction of oxide nanoparticles were estimated by ImageJ Analysis Software.

3. Results

3.1. Microstructures of the powders

Fig. 1 shows the morphologies of the raw powders and as-milled powders. It can be clearly seen that the FeCrNi gas-atomized powders are mainly in a spherical shape, while the TiH_2 and YH_3 powders are predominantly in an irregular shape. Hydrides are inherently brittle and easily broken during ball milling. The particle sizes of the FeCrNi gas-atomized powders, TiH_2 and YH_3 powders are 49.1, 28.2, and 20.8 μm, respectively. After mechanical milling, the morphologies of the raw powders are completely changed. The as-milled powders are in nearly spherical shape, and the average particle size significantly decreases to 14.5 μm. The Y and Ti atoms can be decomposed from raw powders and dissolved into the FeCrNi matrix during the mechanical milling process [19].

3.2. Phase identification

Fig. 2 shows the XRD patterns of the FeCrNi gas-atomized powders, as-milled powders, and extruded ODS FeCrNi MEA. The diffraction peaks of the FeCrNi gas-atomized powders belong to a single-phase FCC structure. After mechanical milling, there are no other diffraction peaks appearing in the XRD pattern of the as-milled powders except for the FCC-diffraction peaks. The diffraction-peaks broadening and diffraction-peak intensity weakening are detected, and all the diffraction peaks shift to left slightly, indicating numerous defects and high internal stress have been introduced in the lattice [19]. The interplanar spacing and lattice distortion slightly increase, which may be attributed to the introduction of the Ti and Y atoms [8]. After HE, it is apparently observed that the diffraction-peak position remains essentially the same. The diffraction peak intensity increases, and the diffraction peak width becomes narrow, which could be caused by the reduction of the defect density and release of the internal stress.

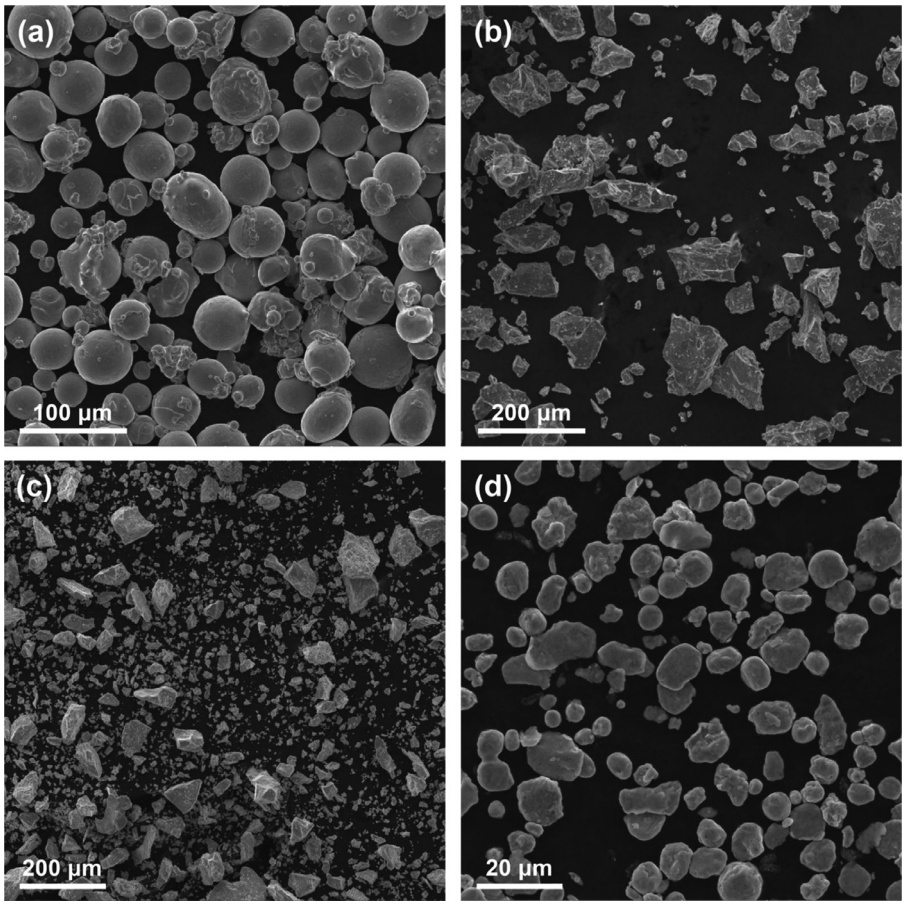

Fig. 1. SEM morphologies of the raw powders and as-milled powders. (a) FeCrNi gas-atomized powders, (b) TiH_2 powders, (c) YH_3 powders, and (d) as-milled powders.

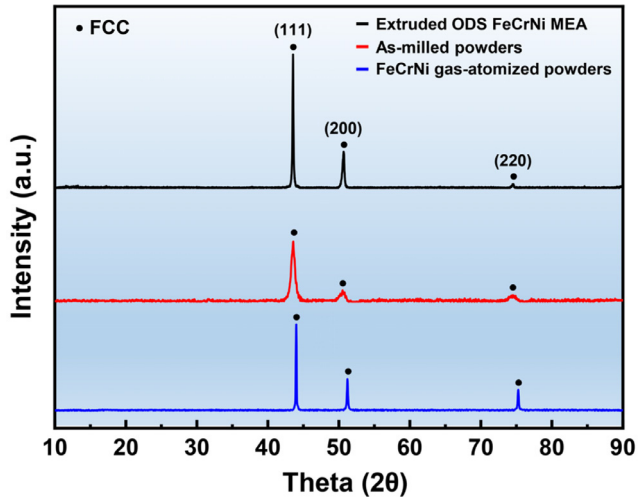

Fig. 2. XRD patterns of the FeCrNi gas-atomized powders, as-milled powders and extruded ODS FeCrNi MEA.

3.3. Microstructure of the extruded ODS FeCrNi MEA

Fig. 3(a) provides the macroscopic image of the extruded bars. Fig. 3(b) and (c) shows the EBSD results of the ODS FeCrNi MEA. The inverse pole figure (IPF) map, shown in Fig. 3(b), confirms that the ODS FeCrNi MEA is composed of fine-equiaxed grains with many annealing twins in the grain interior. The appearance of the annealing twins indicates that the stacking fault energy (SFE) of the matrix alloy is relatively low. Fig. 3(c) shows the average grain size of the ODS FeCrNi MEA is ~318 nm. The grain size of the ODS FeCrNi MEA is significantly refined compared to the MEAs/HEAs fabricated by HE under similar process conditions (e.g., 12 μm for the FeCrNi MEA as shown in Fig. S1) [14,20] because the introduced oxide nanoparticles can effectively retard the grain growth by pinning the movement of grain boundaries [8,9,19].

Fig. 4 shows the TEM images of the ODS FeCrNi MEA. In the bright-field transmission electron microscopy (BF-TEM) image (Fig. 4(a)), the equiaxed grains with annealing twins (indicated by the yellow arrowheads) inside can be clearly observed. A BF-TEM image with higher magnification is presented in Fig. 4(b), revealing that a large number of nearly spherical nanoparticles (indicated by the white arrowheads) with grain sizes from ~2 to ~50 nm are well dispersed in the matrix. The scanning transmission electron microscopy (STEM) images shown in Fig. 4(c) and (d) indicate that the matrix exhibits a bright contrast, and the nanoparticles show a dark contrast. According to the elemental composition analysis results, the nanoparticles are indeed oxides and can be divided into the following two categories: Y-Ti-O typed oxide and Y_2O_3. The energy dispersive spectroscopy (EDS) line scanning in the STEM-1 region (Fig. 4(c)) provides support that the contents of Y, Ti, and O increase while the contents of Fe, Cr, and Ni decrease from the matrix to the nanoparticle, indicating that the nanoparticle is the Y-Ti-O typed oxide. The EDS line scanning in the STEM-2 region (Fig. 4(d)) shows that the contents of Y and O increase while the contents of Fe, Cr, and Ni decrease from the matrix to the nanoparticle. Almost no change in the content of Ti. Therefore, the nanoparticle can be considered to be Y_2O_3. In addition, the EDS elemental mapping presented in Fig. S2 also confirm the existence of the two oxides.

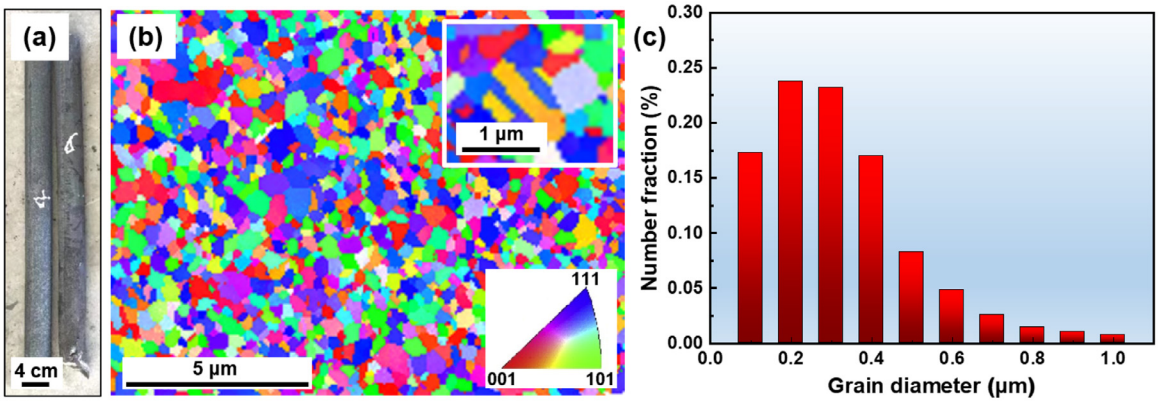

Fig. 3. (a) Macroscopic image of the extruded bars. EBSD characterizations of the extruded ODS FeCrNi MEA: (b) IPF map showing the equiaxed grains and annealing twins, (c) the corresponding grain size distribution in (b).

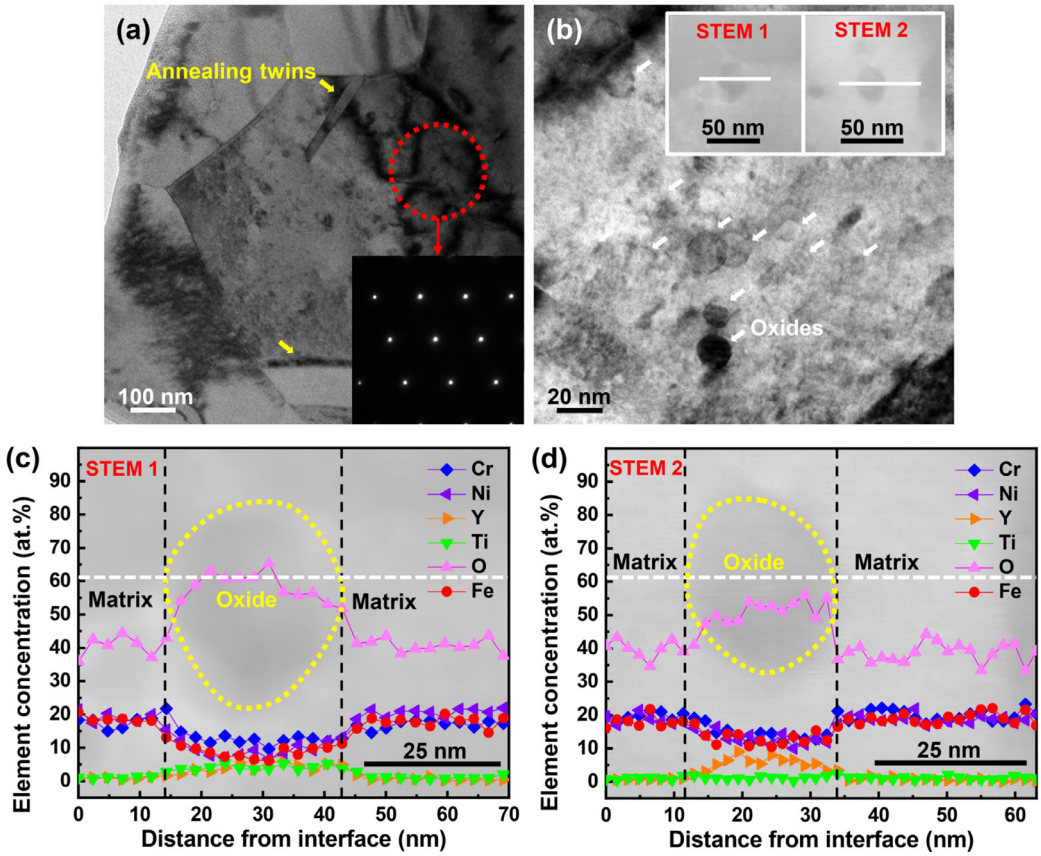

Fig. 4. TEM characterizations of the extruded ODS FeCrNi MEA. (a) BF-TEM image showing the equiaxed grains and annealing twins; (b) BF-TEM image with higher magnification showing the dispersed oxide nanoparticles; STEM images in (c) and (d) showing the EDS line scanning from the matrix to the oxide nanoparticles.

Fig. 5 shows the details of the elemental distribution and particle size of the oxide nanoparticles in the ODS FeCrNi MEA. Fig. 5(a) shows that the Fe, Cr, and Ni are uniformly distributed in the matrix. At the same time, the 1.0 at.% Y isoconcentration surface and 2.0 at.% Y-Ti-O isoconcentration surface are exhibited in Fig. 5(b) and (c) to show the outline of the Y-rich nanoparticles and (Y, Ti, O)-rich nanoparticles, respectively. From the 3D-atom maps, it can be clearly observed that dozens of nearly spherical oxide nanoparticles are well dispersed in the matrix and most of these nanoparticles are simultaneously enriched with Y, Ti, and O. Combined with the TEM observation results, it can be found that the number of (Y, Ti, O)-rich nanoparticles is apparently higher than that of the Y_2O_3 nanoparticles, indicating that the Y-Ti-O typed nanoparticles are the dominant oxides in the ODS FeCrNi MEA. Fig. 5(d) presents a proximity histogram of the elemental distribution profile from the matrix to the oxide nanoparticle in Fig. 5(c), clearly showing that the contents of Fe, Cr, and Ni decrease while the contents of Y, Ti, and O increase from the matrix to the oxide nanoparticle. The corresponding particle-size distribution presented in Fig. 5(e) reveals that the oxide nanoparticles have an average diameter of ~13 nm. Besides, the volume fraction of the oxide nanoparticles can be estimated form dozens of TEM images, and the value is ~0.92 vol.%.

Fig. 6 shows the high-resolution transmission electron microscopy (HRTEM) images of the oxide nanoparticles and the corresponding Fast-Fourier Transformation (FFT) images in the ODS

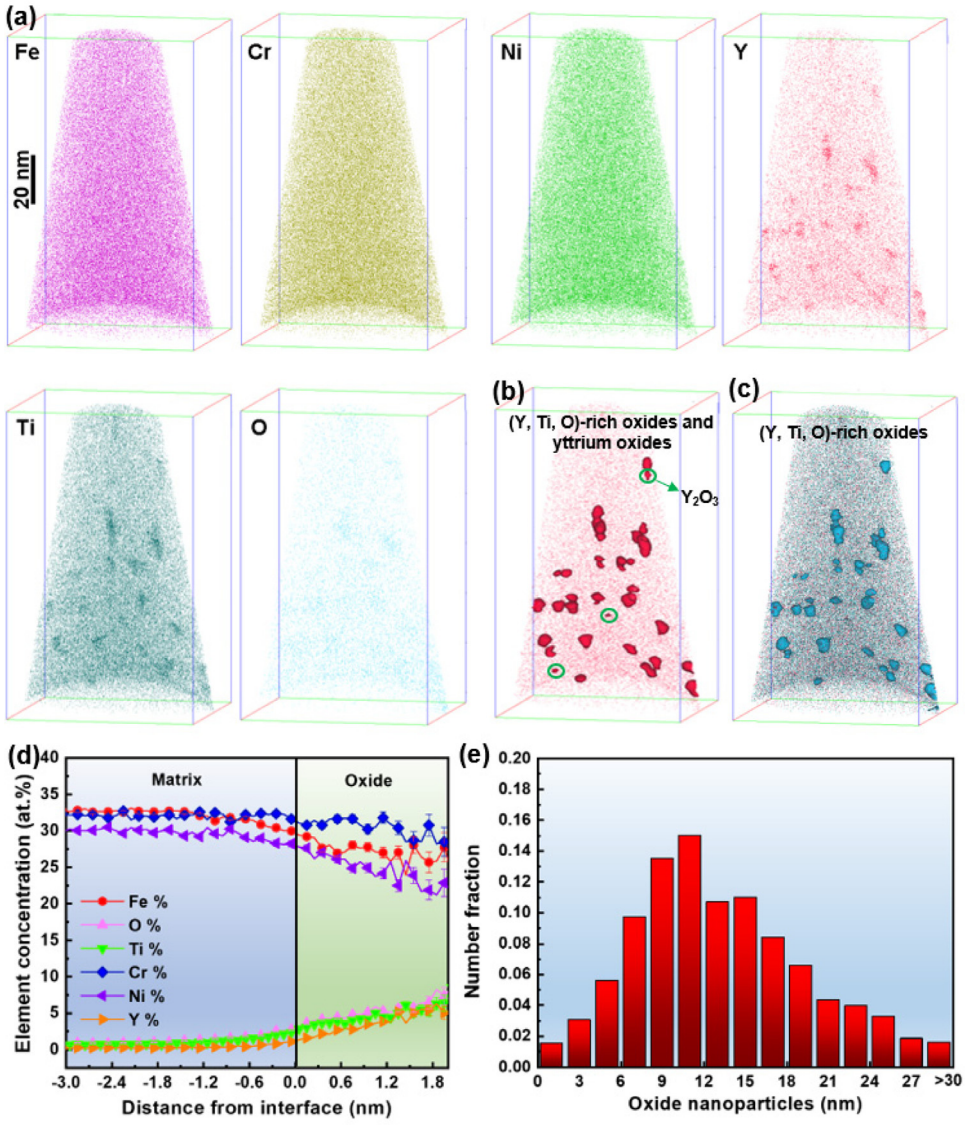

Fig. 5. APT characterizations of the extruded ODS FeCrNi MEA. (a) 3D atom maps showing the elemental distribution of Fe, Cr, Ni, Y, Ti, and O, respectively, at nanoscale; (b) 1.0 at.% Y isoconcentration surface and (c) 2.0 at.% Y-Ti-O isoconcentration surface showing the nearly spherical oxide nanoparticles; (d) elemental distribution profile from the matrix to the oxide nanoparticle in (c); (e) the corresponding particle size distribution of oxide nanoparticles.

FeCrNi MEA. The distance between the yellow parallel lines on the HRTEM images represent the interplanar spacings of the oxide nanoparticles. The yellow and red lines on the FFT images denote the oxide nanoparticles and the matrix, respectively. The oxide nanoparticles with a diameter of ~11.2 nm in Fig. 6(a) are identified as a $Y_2Ti_2O_7$ phase with a pyrochlore FCC structure. Analysis of the corresponding diffractograms reveal a coherent relationship between the $Y_2Ti_2O_7$ phase and the FCC matrix, and the coherent relationships are listed as follows: $[101]_O//[011]_M$, $(040)_O//(\bar{2}00)_M$, and $(\bar{2}22)_O//(\bar{1}\bar{1}1)_M$. Interplanar spacings, $d(1\bar{1}1)_M$, of the FCC matrix and $d(33\bar{3})_P$ of the $Y_2Ti_2O_7$ phase are 0.2108 and 0.1976 nm, respectively. The misfit parameter, δ, can be calculated as ~0.062 (between 0.05 (coherent) and 0.25 (incoherent) [19]), indicating a semi-coherent interface between the $Y_2Ti_2O_7$ phase and the FCC matrix. However, the coherent relationship between the $Y_2Ti_2O_7$ phase and FCC matrix is strongly related with the directions and planes [19,21–23]. Fig. 6(c) shows the spherical nanoparticle with a diameter of ~9.6 nm, and the corresponding FFT image indicates that the nanoparticle is a Y_2TiO_5 phase oriented with [142] zone axis parallel to the electron beam and has an orthorhombic structure. Moreover, a small nanoparticle with a diameter of ~6.4 nm is detected, as shown in Fig. 6(e). The measured interplanar distance and angles reveal that the nanoparticle is a Y_2O_3 phase oriented with the [110] zone axis and has a bixbyite body-centered-cubic (BCC) structure. The oxide nanoparticles, including $Y_2Ti_2O_7$, Y_2TiO_5, and Y_2O_3, have also been found in many ODS materials, especially the ODS steels. Generally, these three types of oxide nanoparticles exhibit a coherent relationship with the γ-Fe matrix composed of single-phase FCC structure [23]. Meanwhile, the coherency between these oxide nanoparticles and the FCC matrix increases with the decrease in the particle size. Therefore, by introducing these fine oxide nanoparticles, the ODS materials can achieve a significant increase in strength and maintain moderate plasticity.

3.4. Tensile properties

Fig. 7(a) shows the tensile engineering stress-strain curves of the ODS FeCrNi MEA, ODS Fe-containing MEAs/HEAs [9,19] and typical ODS austenitic stainless steels [24,25]. The ODS FeCrNi

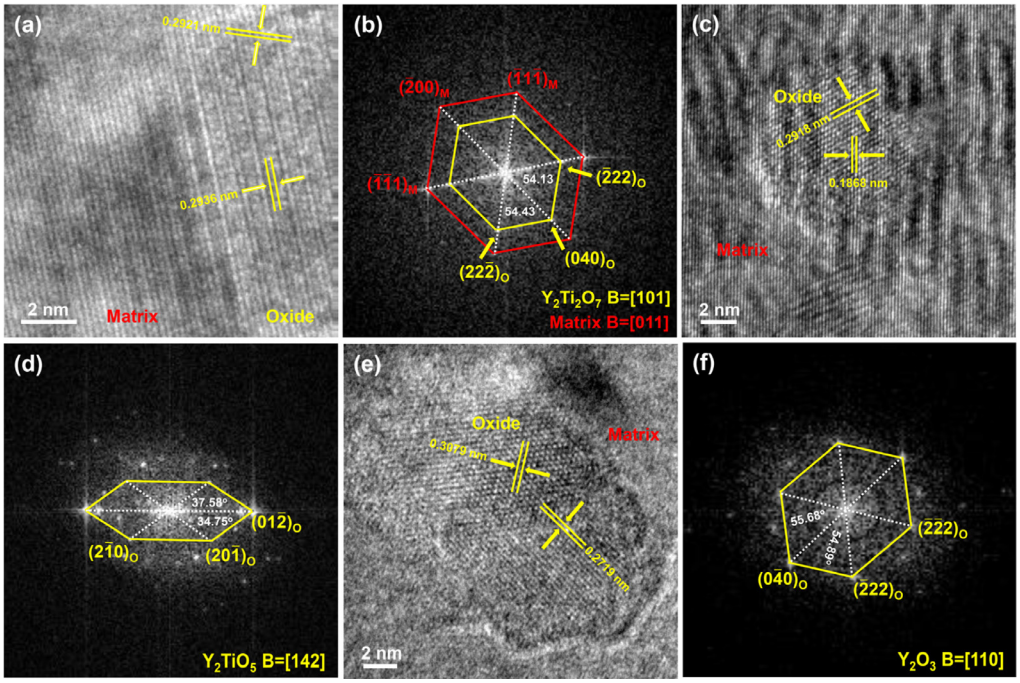

Fig. 6. HRTEM images of different oxide nanoparticles in the extruded ODS FeCrNi MEA. (a) $Y_2Ti_2O_7$ nanoparticle with a diameter of ~11.2 nm; (b) corresponding FFT of (a); (c) Y_2TiO_5 nanoparticle with a diameter of ~9.6 nm; (d) corresponding FFT of (c); (e) Y_2O_3 nanoparticle with a diameter of ~6.4 nm; (f) corresponding FFT of (e).

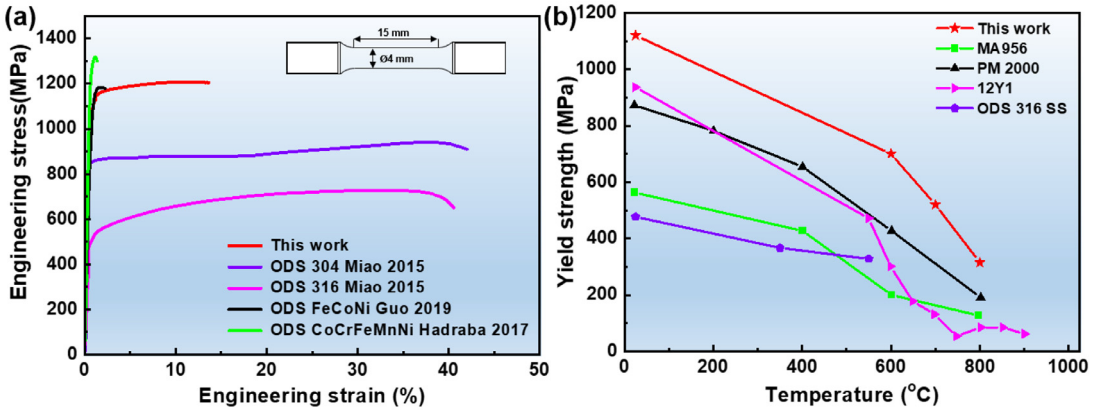

Fig. 7. (a) Tensile properties of the extruded ODS FeCrNi MEA, ODS Fe-containing MEAs/HEAs [9,19]; and typical ODS austenitic stainless steels at room temperature [24,25]; (b) yield strength of the extruded ODS FeCrNi MEA and various ODS steels at different temperatures [25,27].

MEA exhibits high yield strength and ultimate tensile strength along with moderate ductility, and the corresponding values are 1120 MPa, 1274 MPa and 12.1%, respectively. Apparently, the yield strength of the ODS FeCrNi MEA is significantly higher than that of the common steels [24,25], such as ODS 316 stainless steel (477 MPa) and ODS 304 stainless steel (852 MPa), while slight lower than that of the typical ODS Fe-containing MEAs/HEAs [9,19]. However, the fracture elongation is significantly better than that of the typical ODS Fe-containing MEAs/HEAs [9,19], such as ODS FeCoNi MEA (1.2%) and ODS FeCoCrNiMn HEAs (0.74%). In addition, the yield strength and ultimate tensile strength of the ODS FeCrNi MEA are also obviously better than those of the typical ODS CoCrNi MEA (764 MPa and 1129 MPa, respectively) [11], but the fracture elongation is relatively lower, which may be due to the higher density of oxides in the ODS FeCrNi MEA than in ODS CoCrNi MEA. For a better comparison, more detailed comparisons about tensile properties of the ODS FeCrNi MEA, ODS MEAs/HEAs [9,15,19,26] and typical ODS steels [24,25,27–29] are also listed in Table 1, from which it can be seen that the ODS FeCrNi MEA exhibits an outstanding strength and ductility combination, with an improved yield strength of 248 MPa, compared to the PM2000 at a similar elongation. In addition, the high-temperature tensile properties of the ODS FeCrNi MEA and other typical ODS steels [25,27] in a wide temperature range from 25 to 900 °C are plotted in Fig. 7(b). It can be seen that the ODS FeCrNi MEA (indicated by the red line) maintains a high yield strength of 701 MPa at 600 °C and exhibits significant strength advantage at the same tensile temperature than that of the other ODS steels, such as the PM2000.

3.5. Deformation microstructure

Fig. 8 shows a typical room-temperature deformation microstructure of the matrix in the ODS FeCrNi MEA after a tensile test at a strain rate of 1×10^{-3} s^{-1}. As indicated in Fig. 8(a), high density of dislocations pile up at the grain boundaries and annealing twin boundaries. The dislocation slip and deformation-induced twinning are highly activated, as shown in Fig. 8(b) and (c). Numerous nanotwins with an average thickness of tens of nanome-

Table 1
Tensile properties of the ODS FeCrNi MEA, ODS HEAs/MEAs [9,15,19,26] and other typical ODS steels [24,25,27–29].

Materials	Chemical composition	Microstructure[a]	Process[a]	Ultimate tensile strength (MPa)	Yield strength (MPa)	Elongation (%)	Refs.
ODS FeCoCrNiMn	–	FCC	SPS	1318	1269	0.74	[9]
ODS FeCoCrNi	FeCoCrNi-1.2Hf-1.5Y_2O_3	FCC	SPS+HR	1464	1250	1.9	[26]
ODS FeCoNi	FeCoNi-1.2Ti-1.5Y_2O_3	FCC	SPS+HR+AT	1140	1050	1.2	[19]
ODS CoCrNi	CoCrNi-0.4TiO_2	FCC	Arc melting	1129	764	66	[11]
12 YWT	Fe-12.58Cr-2.44W-0.35Ti-0.16Y-0.16O	F/M	HE+HR+WR+AT	1250	1180	5	[27]
ODS Eurofer 97	Fe-0.1C-9Cr-1W-0.2V-0.1Ta-0.3Y_2O_3	F/M	HIP+HR	1085	966	11.7	[28]
ODS 304	Fe-18Cr-8Ni-1Mo-0.5Ti-0.15Si-0.35Y_2O_3	A	HIP+Forge+HR	946	852	42	[24]
MA956	Fe-21.7Cr-5.77Al-0.33Ti-0.38Y-0.33Ti	F	–	547	563	10	[27]
12Y1	Fe-12.85Cr-0.24Ni-0.2Y-0.15O	F/M	HE+HR+Rolling+AT	1004	950	3	[27]
PM2000	Fe-20.01Cr-5.59Al-0.50Y_2O_3–0.51Ti	F	HR	925	790	16	[12]
ODS 310	Fe-23.97Cr-18.33Ni-0.32Ti-1.93Mo-0.26Y-0.16O	A	HIP+Forge+HR+Rolling+AT	852	601	30	[29]
ODS 316	Fe-16.82Cr-13.23Ni-2.48Mo-0.4Mo-0.3Ti-0.35Y_2O_3	A	HIP	729	477	39	[25]
FeCoCrNi	FeCoCrNi	FCC	SPS+AT	1041	978	2.6	[26]
FeCrNi	FeCrNi	FCC	HE	1035	644	54	[14]
FeCoNi	FeCoNi	FCC	SPS+HR+AT	709	559	12.0	[19]
ODS FeCrNi	FeCrNi-0.21Y-0.35Ti-0.529O	FCC	HE	1274	1120	12.1	This work

[a] The following acronyms are used: A (austensitic); F (ferritic); M (martensitic); HIP (hot isostatic pressing); HR (hot rolling); WR (warm rolling); AT (annealing treatment).

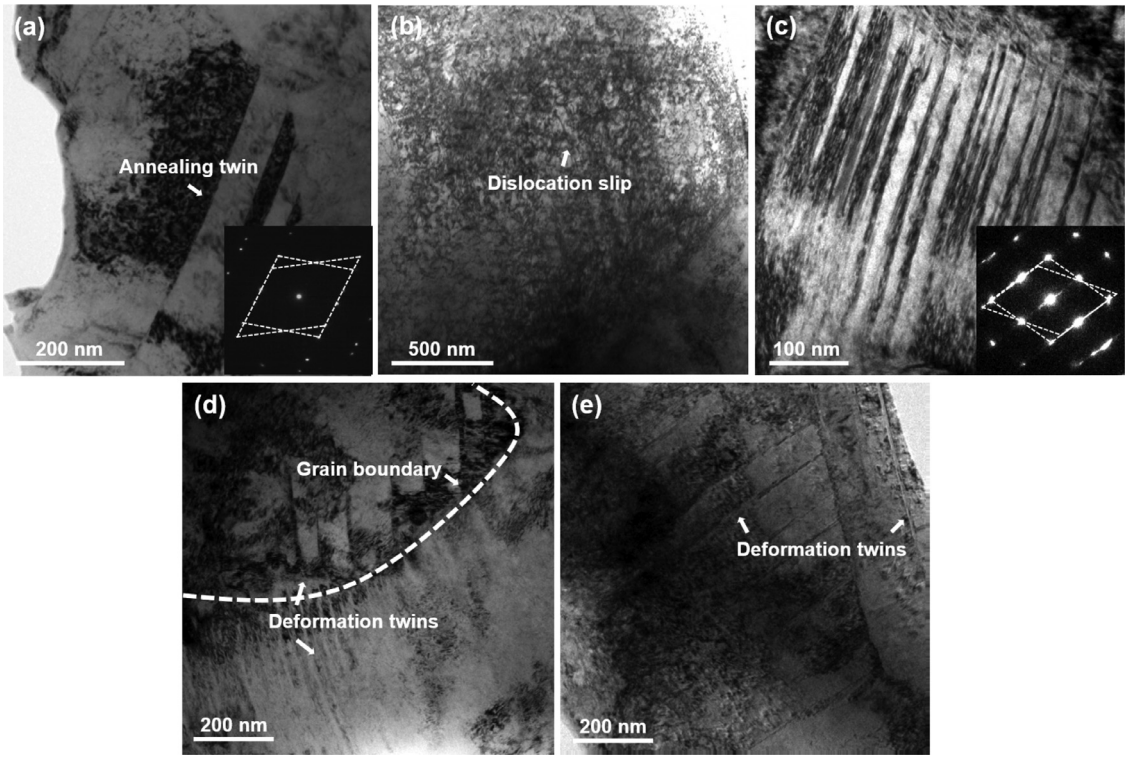

Fig. 8. TEM characterizations of the extruded ODS FeCrNi after a tensile test. BF-TEM images showing (a) the accumulation of high-density dislocations at grain boundaries and annealing-twin boundaries, (b) the dislocation slip, (c, d) the deformation twin regions with thickness of hundreds of nanometers, and (e) the multiple deformation twinning network.

ters can be observed in the grain interior (Fig. 8(d)). Moreover, a large scaled multiple deformation twinning network appears, as exhibited in Fig. 8(e). A high density of deformation microstructures, especially deformation-induced twins, can refine the grain size continuously and present more barriers for limiting the dislocation motion to induce higher strength and stronger strain hardening by the so-called dynamic Hall-Petch effect [14]. Meanwhile, the twinning behavior can also provide adequate pathways for the dislocation glide and cross-slip to relieve stress concentration and accommodate plastic deformation. Therefore, the FCC matrix can guarantee the ODS FeCrNi MEA a good tensile elongation and produce partial strength improvement at the same time.

Fig. 9 shows the deformation behavior related to oxide nanoparticles of the extruded ODS FeCrNi MEA. About dozens of oxide nanoparticles with different diameters are selected to analyze their deformation behavior. Fig. 9(a) shows that the oxide nanoparti-

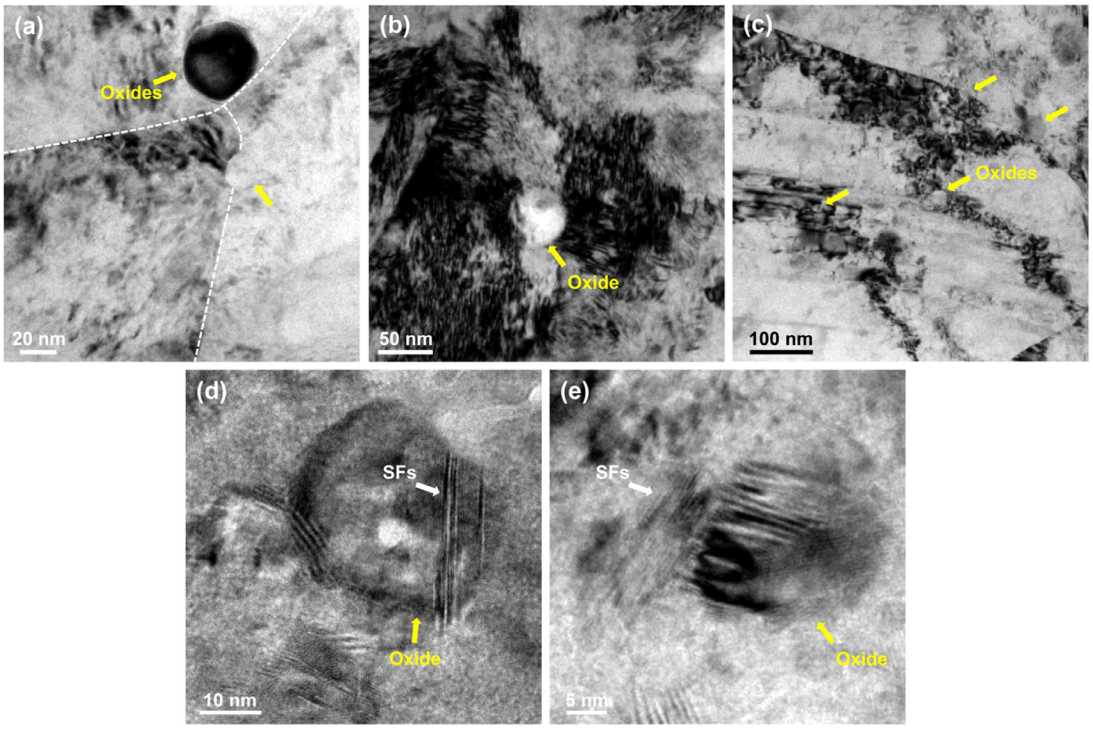

Fig. 9. TEM characterizations of the oxide nanoparticles in the extruded ODS FeCrNi after a tensile test. BF-TEM images showing that (a) the grain boundaries, (b) the dislocations, (c) the deformation twin boundaries are pinned by the oxide nanoparticles, (d) the SFs inside the oxide nanoparticles, and (e) the oxide nanoparticles are sheared.

cles are precipitated at the grain boundaries, which is beneficial to suppress the grain growth during the HE process and lead to the grain refinement. A high density of oxide nanoparticles, especially those inside the grains (Fig. 9(b)), can act as dispersed obstacles to restrict dislocation movement continuously during deformation process, leading to a significant precipitation strengthening. Because the oxide nanoparticles are well dispersed in the matrix, the highly-activated dislocation slip and deformation-induced twinning during the deformation process will inevitably be restricted by these oxide nanoparticles. Fig. 9(c) shows that the twin boundaries are pinned by the oxide nanoparticles marked by yellow arrowheads, and a large number of dislocations are accumulated in the area near the interfaces between the oxide nanoparticles and nanotwins. Fig. 9(d) and (e) shows another interesting deformation feature for oxide nanoparticles. Numerous stacking faults (SFs) indicated by the white arrowhead can be observed inside the oxide nanoparticle. Meanwhile, the smaller oxide nanoparticle with a diameter of ~13 nm presented in Fig. 9(e) exhibits more significant deformation characterizations, and the upper left area of the oxide nanoparticle is severely sheared due to the strong interference from the deformed matrix. Since the interfacial coherency between the oxide nanoparticles and FCC matrix increases with the decrease in the particle size [22], the smaller oxide nanoparticles tend to be more sensitive to plastic deformation. Previous studies [22,30] found that the $YAlO_3$ nanoparticles with diameters smaller than 20 nm and the $Y_2Ti_2O_7$ with diameters smaller than 10 nm are appreciably deformed when they undergo severe plastic deformation, and their morphologies change from a spherical to oblate shape. The deformation-induced shearing and twinning are considered as the dominant deformation mechanism for these oxide nanoparticles, such as $YAlO_3$ and $Y_2Ti_2O_7$ [21,30]. However, most large oxide nanoparticles remain nearly spherical without appreciable plastic deformation.

Fig. 10 presents the fracture morphologies of the extruded ODS FeCrNi MEA after a tensile test. Numerous fine and deep dimples are observed, revealing typical ductile fractures. Moreover, fine particles (marked by white arrowheads) could be found at the bottom of some dimples, and these particles may act as nucleation sites of microvoids or microcracks during tensile deformation. The microvoids and microcracks grow and coalesce with continuously increased deformation strains, which will finally lead to the failure of the ODS FeCrNi MEA.

3.6. Irradiation resistance

Fig. 11(a) shows the full view of microstructure of the ODS FeCrNi MEA irradiated with a fluences of 5×10^{16} Au ions/cm^2. Variation of irradiation damage and Au ions concentration versus depth from the surface are also plotted in Fig. 11(a) for a better comparison. The elemental distribution mapping in Fig. 11(b) shows the Au ions concentration as a function of implantation depth from the surface of the ODS FeCrNi MEA. Obviously, the Au element is mainly concentrated in a narrow range from 580 nm and 1108 nm, which is slightly deeper than the SRIM simulation result. TEM images in Fig. 11(a) and (c) show that small-sized dislocation loops and defect clusters that look like black dots are the main defects in the ODS FeCrNi MEA. The overall distribution of defects is relatively uniform, but the defect density in the high damage area is slightly higher than that in the near-surface area. The introduction of oxides nanoparticles can pin the irradiation-induced defects and inhibit their migration or accumulation, favoring the formation of fine and diffuse defects. The SAED patten along z = [001] axe in the peak damage region (Fig. 11(c)) reveals that the ODS FeCrNi MEA maintains a single-phase FCC structure after irradiation and the diffraction rings corresponding to amorphous structure is absent, showing outstanding phase stability and amorphization resistance. In contrast, most of the traditional alloys, such as nuclear grade steels, refractory metals and intermetallics are easily amorphized at a low irradiation dose [31]. In addition, the irradiation-induced segregation behavior is investi-

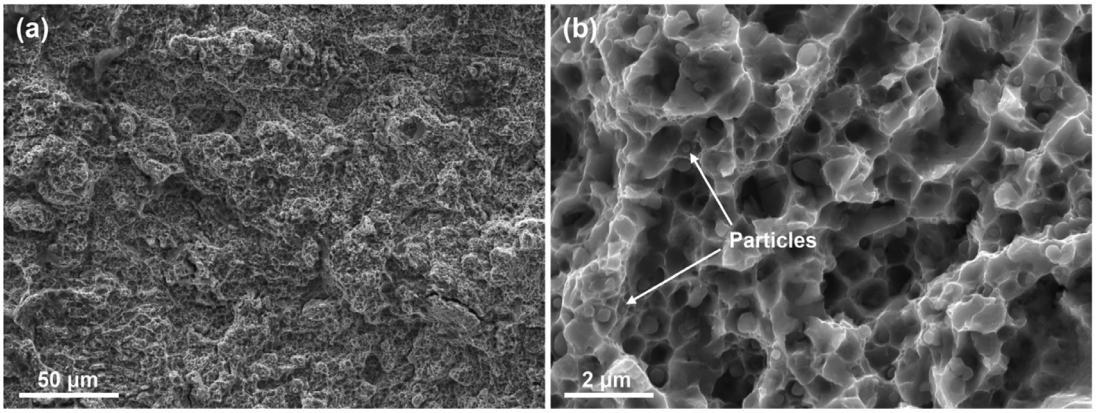

Fig. 10. Fracture morphologies of the extruded ODS FeCrNi MEA after a tensile test. (a) SEM image showing large-scaled dimples; (b) enlarged view presenting the fine dimples and particles.

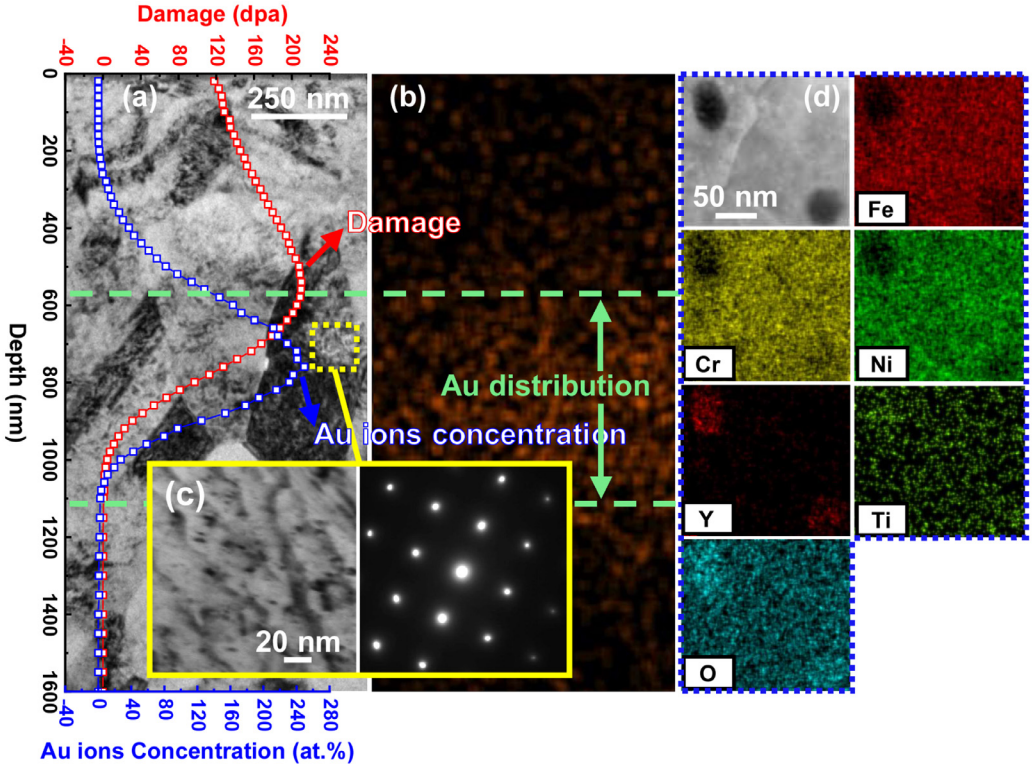

Fig. 11. TEM images showing the full view of the ODS FeCrNi MEA irradiated with a fluences of 5 × 10^{16} Au ions/cm^2. (a) Variation of irradiation damage (indicated by the red line) and Au ions concentration (indicated by the blue line) versus depth from the surface. (b) Elemental mapping showing the Au ions distribution. (c) BF-TEM image with higher magnification showing the dislocation loops and defect clusters; (d) STEM image and the corresponding elemental distribution mapping in the high damage region.

gated in the peak damage region, and no irradiation-induced segregation or secondary phase precipitation is observed at the grain boundaries (Fig. 11(d)). However, the irradiation-induced segregation behavior has been found in many materials, such as CoCrFeNi HEA [32], FeCrMnNi HEA [5], and FeCrNi austenitic stainless steels [32]. The oxide nanoparticles in the peak damage region remain spherical with no significant morphological changes, exhibiting excellent structural stability. Generally, ODS materials can provide abundant grain boundaries and oxide nanoparticle interfaces, which can promote the uniformity of solute diffusion and interstitial/vacancy recombination [33], thereby suppressing irradiation-induced solute enrichment and depletion. Hence, these results indicate that the ODS FeCrNi MEA exhibits excellent irradiation resistance.

4. Discussion

4.1. Strengthening mechanism

Since the mechanical properties and related microstructures of the ODS FeCrNi MEA have been investigated in detail, it is possible to estimate the room-temperature strength. For nanoparticles-strengthened metallic materials, their strengthening mechanism mainly involves the solid-solution strengthening (σ_S), grain-boundary strengthening (σ_G) and precipitation strengthening (σ_P). Hence, the yield strength (σ_y) for the ODS FeCrNi MEA can be simply calculated by the following equation: $\sigma_y = \sigma_0 + \sigma_S + \sigma_G + \sigma_P$, where σ_0 is the lattice friction strength for the FeCrNi MEA. According to the studies reported by Liang

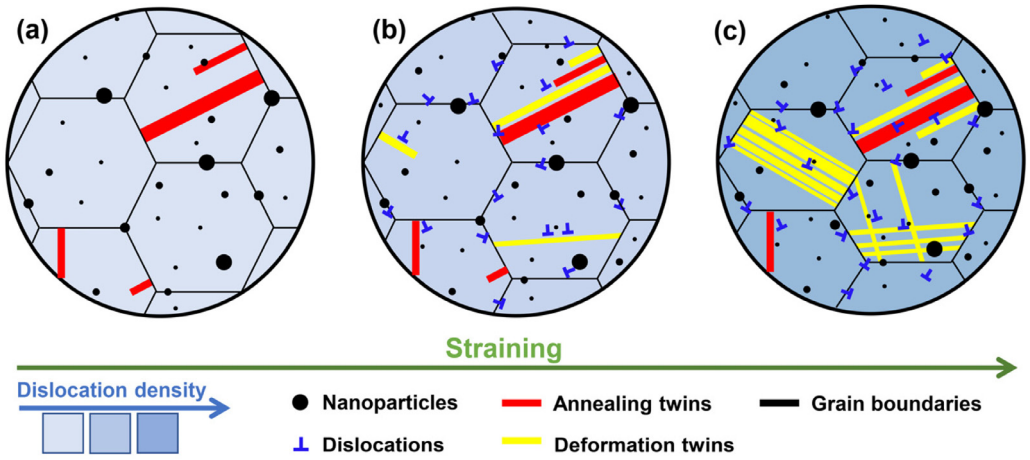

Fig. 12. Schematic diagram of the microstructural evaluation of the ODS FeCrNi HEA during the deformation process and the darker blue in the background indicating the higher dislocation density. (a) Microstructural features before tensile deformation; (b) at the onset of tensile deformation, a large number of dislocations are accumulated along the oxide nanoparticles or grain boundaries. The dislocation density around the grain boundaries, annealing boundaries and oxide nanoparticles, significantly increases. Meanwhile, the dislocation slip and deformation-induced twinning are activated; (c) the deformation-induced twinning is more activated with the continuous increase of tensile strain, resulting in the increase of the twin thickness and much denser nanotwins. At the same time, multiple deformation twinning network occurs extensively in the interior of the grains.

et al. [15,34], the strength contributions from the lattice friction and solid-solution strengthening in the FeCrNi MEA is between 270 MPa and 450 MPa. Considering that the atomic radii of Y and Ti are much larger than those of Fe, Cr, and Ni, the solid-solution strengthening effect of the ODS FeCrNi MEA will be stronger, so the sum of the strength contributions from the lattice friction and solid-solution strengthening of the ODS FeCrNi MEA is considered to be 450 MPa.

Grain boundaries play an important role during the deformation process, and the smaller grain size can offer a higher volume fraction of grain boundaries, resulting in further impediment of dislocation motion. The materials fabricated by HE always have a much finer grain size than that fabricated by other preparation techniques. In addition, the oxide nanoparticles located at the grain boundaries can also effectively suppress the grain growth [19]. For the grain-boundary strengthening mechanism, the improved strength can be estimated by the following Hall-Petch relationship [19,34]: $\sigma_G = k_y/\sqrt{d}$, where k_y is the Hall-Petch coefficient for the FeCrNi MEA [35], and the value is in a range of 110–200 MPa μm1/2 [34,35]; d = 0.318 μm is the average grain size for the ODS FeCrNi MEA. Therefore, the strength contribution from grain-boundary strengthening of the ODS FeCrNi MEA is between 195.1 and 354.7 MPa. In contrast, the grain size of the FeCrNi MEA prepared under the same process condition is 12 μm, and the strength contribution from grain-boundary strengthening is between 35.8 and 57.7 MPa. It can be seen that the grain-boundary contribution in the ODS FeCrNi MEA is significantly higher than that in the FeCrNi MEA.

Meanwhile, nanoparticles can effectively enhance the strength of materials by the bypass (Orowan) or shearing mechanism because they can act as barriers for limiting the dislocation movement during deformation process [19]. Since the oxide nanoparticles in the ODS materials has a high hardness, the Orowan mechanism is expected to control precipitation strengthening, and the strength contribution from this mechanism can be predicted by the following equation [19,36]:

$$\Delta\sigma_P = 0.84\frac{MGb}{2\pi r\sqrt{1-\nu\left(\sqrt{\frac{3\pi}{2f}}-\frac{\pi}{4}\right)}}\ln\left(\frac{\pi r}{4b}\right),$$

where M = 3.06 is Taylor factor for FCC alloys; G is the shear modulus, and the value is adopted as 69 GPa [15]; b = 0.254 is Burgers vector for the FeCrNi MEA [37]; ν = 0.3 is Poisson's ratio [15]; r = 6.5 nm, and f = 0.92 vol.% are the average radius and volume fraction, respectively, of the oxide nanoparticles in the ODS FeCrNi MEA. Thus, strength contribution from precipitation strengthening is calculated as 181.1 MPa.

The above discussion indicates that the high yield strength of the ODS FeCrNi MEA mainly originates from the grain-boundary strengthening caused by the fine grains and the precipitation strengthening caused by the highly dispersed oxide nanoparticles. However, there are still some factors, such as the interstitial oxygen atoms and the interactions of dislocations and twins, which may affect the estimation of the strength contributions.

4.2. Microstructural evolution

Based on the above experimental observations, the microstructural evolution of the ODS FeCrNi MEA during the deformation process can be described as follows. The initial microstructure of the ODS FeCrNi MEA is composed of fine equiaxed grains, annealing twins and highly dispersed oxide nanoparticles, as shown in Fig. 12(a). At the beginning of deformation, plenty of dislocations are accumulated along the grain boundaries and annealing twin boundaries, as presented in Fig. 12(b). The dispersed oxide nanoparticles in the matrix provide a huge number of nanoscale barriers for hindering the dislocation motion, thereby leading to an enhanced strength and strain hardening. The dislocation slip and deformation-induced twinning are activated in this period and preferentially occur in the areas adjacent to the annealing-twin boundaries. As the deformation strain further increases, deformation-induced twinning becomes more activated, producing much denser nanotwins, as shown in Fig. 12(c). The multiple deformation-twinning network occurs extensively in the interior of the grains at the same time. The oxide nanoparticles have a strong interaction with these constantly formed twin boundaries and provide persistent strong barriers to the twin boundaries migration, which may result in partial increases in the strength and strain hardening. Meanwhile, deformation-induced twinning, especially the multiple deformation-twinning network, can provide adequate pathways for dislocation glide and cross-slip to relieve stress concentration and accommodate plastic deformation for rendering a moderate tensile ductility for the ODS FeCrNi MEA. These results clearly suggest that superior mechanical properties can be

achieved by coupling the MEAs/HEAs' advantages and the oxide-dispersion-strengthening effect.

5. Conclusions

In the present work, a novel Co-free ODS FeCrNi MEA was successfully fabricated by the P/M method. Minor introductions of Y, Ti, and O elements in the matrix can induce the in-situ formation of oxide nanoparticles, leading to an improved strength. The effects of the oxide nanoparticles on the deformation behavior and irradiation resistance were investigated, and the main conclusions can be summarized as follow:

(1) The ODS FeCrNi MEA consists of an FCC matrix, in which a high density of oxide nanoparticles, including $Y_2Ti_2O_7$, Y_2TiO_5, and Y_2O_3, are uniformly distributed. Compared with the FeCrNi MEA, the average grain size of the ODS FeCrNi MEA is significantly refined to ~318 nm benefited from by the oxide nanoparticles.
(2) The ODS FeCrNi MEA exhibits a high yield strength (1120 MPa) and ultimate tensile strength (1274 MPa) with adequate ductility retention (12.1%) at 25 °C, and the yield strength is nearly double that of FeCrNi MEA prepared by the same process condition. At the same time, the ODS FeCrNi MEA still maintains a high yield strength of 701 MPa at 600 °C, which is superior, compared with common ODS steels, such as the PM2000.
(3) The enhanced strength for the ODS FeCrNi MEA originates from the grain-boundary strengthening and precipitation strengthening caused by the fine grains and the highly dispersed oxide nanoparticles, respectively. Meanwhile, the moderate elongation can be attributed to the ductile matrix.
(4) High density of oxide nanoparticles can disperse the defect distribution and suppress the defect growth and irradiation-induced segregation, which is the main reason for the excellent irradiation resistance of the ODS FeCrNi MEA. This study provides an effective approach to improve the mechanical properties and irradiation resistance of the MEAs/HEAs by introducing fine oxide nanoparticles, making them to be potential materials for nuclear energy applications.

Originality statement

I write on behalf of myself and all co-authors to confirm that the results reported in the manuscript are original and neither the entire work, nor any of its parts have been previously published. The authors confirm that the article has not been submitted to peer review, nor has been accepted for publishing in another journal. The author(s) confirms that the research in their work is original, and that all the data given in the article are real and authentic. If necessary, the article can be recalled, and errors corrected.

Declaration of Competing Interest

The authors declare that they have no known competing financial interests or personal relationships that could have appeared to influence the work reported in this paper.

Acknowledgements

This work was supported by the National Natural Science Foundation of China (Nos. 52020105013 and 52104365), and the US National Science Foundation (Nos. DMR 1611180 and 1809640) with program directors, Drs. J. Yang, G. Shiflet, and D. Farkas.

Supplementary materials

Supplementary material associated with this article can be found, in the online version, at doi:10.1016/j.jmst.2022.11.061.

References

[1] T. Allen, J. Busby, M. Meyer, D. Petti, Mater. Today 13 (2010) 14–23.
[2] S. Peng, Z. Lu, L. Yu, J. Alloys Compd. 861 (2021) 157940.
[3] X. Yan, X. Zhang, F. Wang, T. Stockdale, Y. Dzenis, M. Nastasi, B. Cui, JOM 71 (2019) 2856–2867.
[4] C. Parkin, M. Moorehead, M. Elbakhshwan, J. Hu, W. Chen, M. Li, L. He, K. Sridharan, A. Couet, Acta Mater. 198 (2020) 85–99.
[5] N.A.P.K. Kumar, C. Li, K.J. Leonard, H. Bei, S.J. Zinkle, Acta Mater. 113 (2016) 230–244.
[6] V.N. Voyevodin, S.A. Karpov, G.D. Tolstolutskaya, M.A. Tikhonovsky, A.N. Velikodnyi, I.E. Kopanets, G.N. Tolmachova, A.S. Kalchenko, R.L. Vasilenko, I.V. Kolodiy, Philos. Mag. 100 (2020) 822–836.
[7] L. Yang, H. Ge, J. Zhang, T. Xiong, Q. Jin, Y. Zhou, X. Shao, B. Zhang, Z. Zhu, S. Zheng, X. Ma, J. Mater. Sci. Technol. 35 (2019) 300–305.
[8] Y. Guo, M. Li, C. Chen, P. Li, W. Li, Q. Ji, Y. Zhang, Y. Chang, Intermetallics 117 (2020) 106674.
[9] H. Hadraba, Z. Chlup, A. Dlouhy, F. Dobes, P. Roupcova, M. Vilemova, J. Matejicek, Mater. Sci. Eng. A 689 (2017) 252–256.
[10] F. Dobeš, H. Hadraba, Z. Chlup, A. Dlouhý, M. Vilémová, J. Matějíček, Mater. Sci. Eng. A 732 (2018) 99–104.
[11] W.C. Chang, Y.C. Lu, C.H. Hsueh, Mater. Sci. Eng. A 859 (2022) 144196.
[12] J.L. González-Carrasco, G. Ciapetti, M.A. Montealegre, S. Pagani, J. Chao, N. Baldini, Biomaterials 26 (2005) 3861–3871.
[13] H. Cheng, W. Chen, X. Liu, Q. Tang, Y. Xie, P. Dai, Mater. Sci. Eng. A 719 (2018) 192–198.
[14] A. Fu, B. Liu, W. Lu, B. Liu, J. Li, Q. Fang, Z. Li, Y. Liu, Scr. Mater. 186 (2020) 381–386.
[15] D. Liang, C. Zhao, W. Zhu, P. Wei, F. Jiang, Y. Zhang, Q. Sun, F. Ren, Mater. Sci. Eng. A 762 (2019) 138107.
[16] C. Li, X. Hu, T. Yang, N.A.P.K. Kumar, B.D. Wirth, S.J. Zinkle, J. Nucl. Mater. 527 (2019) 151838.
[17] Y. Xie, D. Zhou, Y. Luo, T. Xia, W. Zeng, C. Li, J. Wang, J. Liang, D. Zhang, Mater. Charact. 148 (2019) 307–316.
[18] Y. Liu, J. Chen, Z. Li, X. Wang, P. Zhang, J. Liu, Vacuum 184 (2021) 109882.
[19] Y. Guo, M. Li, P. Li, C. Chen, Q. Zhan, Y. Chang, Y. Zhang, J. Alloys Compd. 820 (2020) 153104.
[20] B. Liu, J. Wang, Y. Liu, Q. Fang, Y. Wu, S. Chen, C.T. Liu, Intermetallics 75 (2016) 25–30.
[21] D. Litvinov, A. Chauhan, T. Gräning, J. Aktaa, Materialia 5 (2019) 100176.
[22] E. Aydogan, O. El-Atwani, S. Takajo, S.C. Vogel, S.A. Maloy, Acta Mater. 148 (2018) 467–481.
[23] X. Mao, K.H. Oh, S.H. Kang, T.K. Kim, J. Jang, Acta Mater. 89 (2015) 141–152.
[24] Y. Miao, K. Mo, Z. Zhou, X. Liu, K.C. Lan, G. Zhang, M.K. Miller, K.A. Powers, J. Almer, J.F. Stubbins, Mater. Sci. Eng. A 625 (2015) 146–152.
[25] Y. Miao, K. Mo, Z. Zhou, X. Liu, K.C. Lan, G. Zhang, M.K. Miller, K.A. Powers, Z. Mei, J. Park, J. Almer, J.F. Stubbins, Mater. Sci. Eng. A 639 (2015) 585–596.
[26] M. Li, Y. Guo, H. Wang, J. Shan, Y. Chang, Intermetallics 123 (2020) 106819.
[27] R.L. Klueh, J.P. Shingledecker, R.W. Swindeman, D.T. Hoelzer, J. Nucl. Mater. 341 (2005) 103–114.
[28] D.T. Hoelzer, M.A. Sokolov, M.A. Sokolov, Z. Feng, J. Nucl. Mater. 442 (2013) S529–S534.
[29] Z. Zhou, S. Sun, L. Zou, Y. Schneider, S. Schmauder, M. Wang, Fusion Eng. Des. 138 (2019) 175–182.
[30] Z. Zhang, W. Pantleon, Acta Mater. 149 (2018) 235–247.
[31] M. Sadeghilaridjani, A. Ayyagari, S. Muskeri, V. Hasannaeimi, R. Salloom, W. Chen, S. Mukherjee, J. Nucl. Mater. 529 (2020) 151955.
[32] C. Lu, T. Yang, K. Jin, N. Gao, P. Xiu, Y. Zhang, F. Gao, H. Bei, W.J. Weber, K. Sun, Y. Dong, L. Wang, Acta Mater. 127 (2017) 98–107.
[33] G. Pu, L. Lin, R. Ang, K. Zhang, B. Liu, B. Liu, T. Peng, S. Liu, Q. Li, Appl. Surf. Sci. 516 (2020) 146129.
[34] D. Liang, C. Wei, F. Ren, Mater. Sci. Eng. A 30 (2020) 140611.
[35] Z. Wu, H. Bei, F. Otto, G.M. Pharr, E.P. George, Intermetallics 46 (2014) 131–140.
[36] J.Y. He, H. Wang, H.L. Huang, X.D. Xu, M.W. Chen, Y. Wu, X.J. Liu, T.G. Nieh, K. An, Z.P. Lu, Acta Mater. 102 (2016) 187–196.
[37] G. Laplanche, P. Gadaud, C. Bärsch, K. Demtröder, C. Reinhart, J. Schreuer, E.P. George, J. Alloys Compd. 746 (2018) 244–255.